Ultra-low dielectric constant amorphous boron nitride

Seokmo Hong[1], Chang-Seok Lee[5], Min-Hyun Lee[5], Yeongdong Lee[3,9], Kyung Yeol Ma[2,9], Gwangwoo Kim[1], Seong In Yoon[2,9], Kyuwook Ihm[6], Ki-Jeong Kim[6], Tae Joo Shin[7], Sang Won Kim[5], Eun-Chae Jeon[10], Hansol Jeon[3], Ju-Young Kim[3], Hyung-Ik Lee[8], Zonghoon Lee[3,9], Aleandro Antidormi[11], Stephan Roche[11,12], Manish Chhowalla[13], Hyeon-Jin Shin[5], and Hyeon Suk Shin[1,2,4,9]

[1]Department of Chemistry, [2]Department of Energy Engineering, [3] School of Materials Science and Engineering and [4]Low-Dimensional Carbon Materials Center, Ulsan National Institute of Science and Technology (UNIST), Ulsan 44919, Republic of Korea

[5]Inorganic Material Lab., Samsung Advanced Institute of Technology (SAIT), Suwon 433-803, Republic of Korea

[6]Pohang Accelerator Laboratory, Kyungbuk 37673, Republic of Korea

[7]UNIST Central Research Facilities & School of Natural Science, Ulsan 44919, Republic of Korea

[8]Analytical Engineering Group, Samsung Advanced Institute of Technology (SAIT), Suwon 433-803, Republic of Korea

[9]Center for Multidimensional Carbon Materials, Institute for Basic Science (IBS), Ulsan 44919, Republic of Korea

[10]School of Materials Science and Engineering, University of Ulsan, Ulsan 44610, Republic of Korea

[11]Catalan Institute of Nanoscience and Nanotechnology (ICN2), CSIC and BIST, Campus UAB, Bellaterra, Barcelona, Spain

[12]ICREA, Institucio Catalana de Recerca i Estudis Avancats, Barcelona, Spain

[13]Department of Materials Science and Metallurgy, University of Cambridge, Cambridge, UK

Corresponding authors: HSS (shin@unist.ac.kr), HJS (hyeonjin.shin@samsung.com) and MC (mc209@cam.ac.uk)

The decrease in signal processing speed due to increased resistance and capacitance delay resulting from aggressive miniaturisation of logic and memory devices is a major obstacle for continued down scaling of electronics.[1-3] In particular, minimizing the dimensions of interconnects – metal wires that connect different device components on the chip – is crucial for device scaling. The interconnects are isolated from each other by non-conducting or dielectric layers. Much of the recent research has focused on decreasing the resistance of scaled interconnects because integration of dielectrics using complementary metal oxide semiconductor (CMOS) compatible processes has proven to be exceptionally challenging. The key requirements for interconnect isolation materials are that they should possess low relative dielectric constants (referred to as κ–values), serve as diffusion barriers against migration of interconnect metals such as cobalt into semiconductors and be thermally, chemically and mechanically stable. In 2005, the International Roadmap for Devices and Systems (IRDS) recommended dielectrics with κ-values of < 2.2 and the most recent report recommends dielectric values of ≤ 2 by 2028.[4] Despite this, state-of-the-art low-κ materials, such as silicon oxide derivatives, organic compounds, and aerogels exhibit κ values > 2 and possess poor thermo-mechanical properties.[5] Here, we report a dielectric thin film with ultra-low κ values of 1.78 and 1.16 – close to that of air (κ = 1) – at 100 kHz and 1 MHz, respectively, in amorphous boron nitride (a-BN) obtained using CMOS compatible low temperature process. We demonstrate that 3 nm thin a-BN is mechanically and electrically robust with breakdown strength of 7.3 MV/cm – exceeding requirements. Cross-sectional transmission electron microscopy reveals that a-BN is able to prevent diffusion of cobalt interconnect atoms into silicon under very harsh accelerated conditions – in contrast with

reference barriers. Our results demonstrate that the amorphous counterpart of two-dimensional hexagonal BN possesses the ideal low-κ dielectric characteristics for high-performance electronics.

Modern high-performance logic and memory devices used in multifunctional electronics are obtained by materials and design innovations that have enabled aggressive reduction of transistor size and packing of more circuits in smaller areas.[1-3,6-11] However, the reduction in dimensions of metal interconnects and increased packing density has led to an increase in resistance – capacitance (*RC*) delay that is becoming comparable to operation speed of the devices. Ideally, both *R* and *C* should be simultaneously reduced for continuous scaling of devices. However, development of electrically, mechanically and thermally robust low-κ materials ($\kappa < 2$) using CMOS compatible processes that are good inter-metal and inter-layer dielectrics as well as diffusion barriers against electro-migration of metal atoms from interconnects has been challenging.

State-of-the-art strategies for achieving low-κ dielectrics have involved reducing the polarisation strength and density of SiO_2 ($\kappa = 4$) by incorporation of fluorine ($\kappa = 3.7$ for SiOF) or CH_3 ($\kappa = 2.8$ for SiCOH) and introducing porosity (porous SiCOH or pSiCOH possess $\kappa = 2.4$).[1,12] The realisation of IRDS recommendations for 2028 calls for urgent development of ultra-low-κ dielectrics with κ-values of less than 2.[13,14] IRDS has also indicated that the greatest challenge concerning interconnect development is the introduction of new materials with reduced dielectric permittivity. Boron-based compounds such as BCN and amorphous BN (a-BN) have been investigated as potential low-κ dielectrics – showing promising results.[5] However, recent reports on BN dielectrics show films with turbostratic structure or high

dielectric constants that indicate crystalline structure.[15,16] In this study, we utilized low temperature inductively coupled plasma–chemical vapour deposition (ICP-CVD, see Methods and Extended Data Fig. 1) to obtain 3 nm thick BN layers on Si substrates (See Extended Data Fig. 2 for growth on Cu and SiO_2 substrates). Transmission electron microscopy imaging and diffraction results shown in Fig. 1 reveal that the films are amorphous with no discernible long-range order – hence we refer to them as amorphous BN (a-BN). Cross-sectional chemical mapping confirms that the films consist of B and N (Extended Data Fig. 3). X-ray photoelectron spectroscopy (XPS) was used to obtain chemical information. The B/N atomic ratio was found to be ~ 1:1.08 (Fig. 2a and b) with B 1s and N 1s peaks at 190.4 eV and 397.9 eV, respectively, – indicating that the films are sp^2-bonded B and N.[17,18] Molecular dynamics simulations shown in Extended Data Fig. 4 confirm the amorphous structure of BN films which is consistent with the result in Fig. 1.

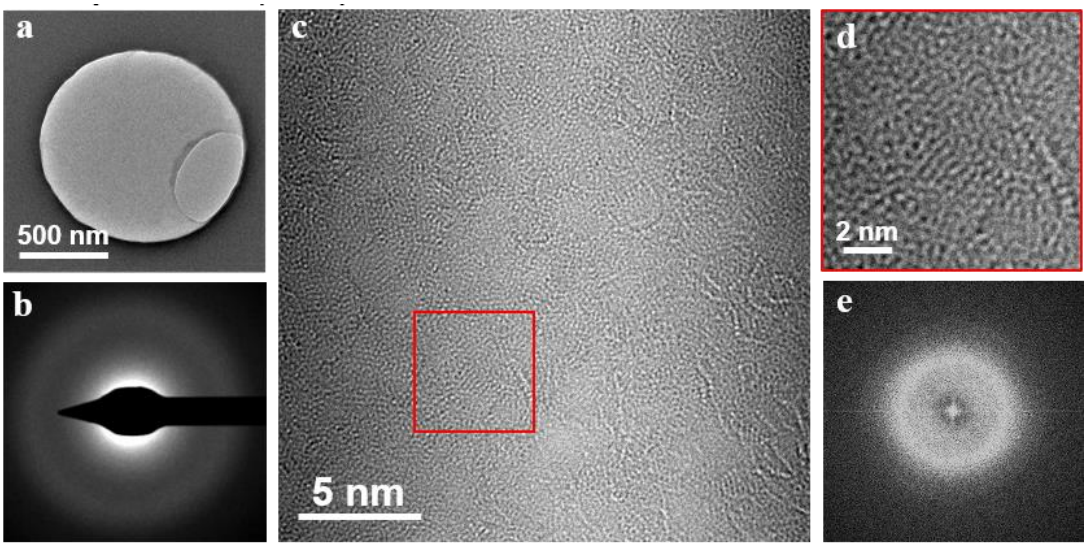

Fig. 1 | Atomic structure of amorphous boron nitride. (a) Low-magnification TEM image; (b) Selective area electron diffraction showing diffuse pattern with no discernible crystalline rings; (c) High-resolution TEM image; (d) Magnified image of red box in (c) demonstrating disordered atomic arrangement; (e) Fast Fourier Transform results for area depicted in (d)

demonstrating diffuse diffraction pattern that is typical of an amorphous film.

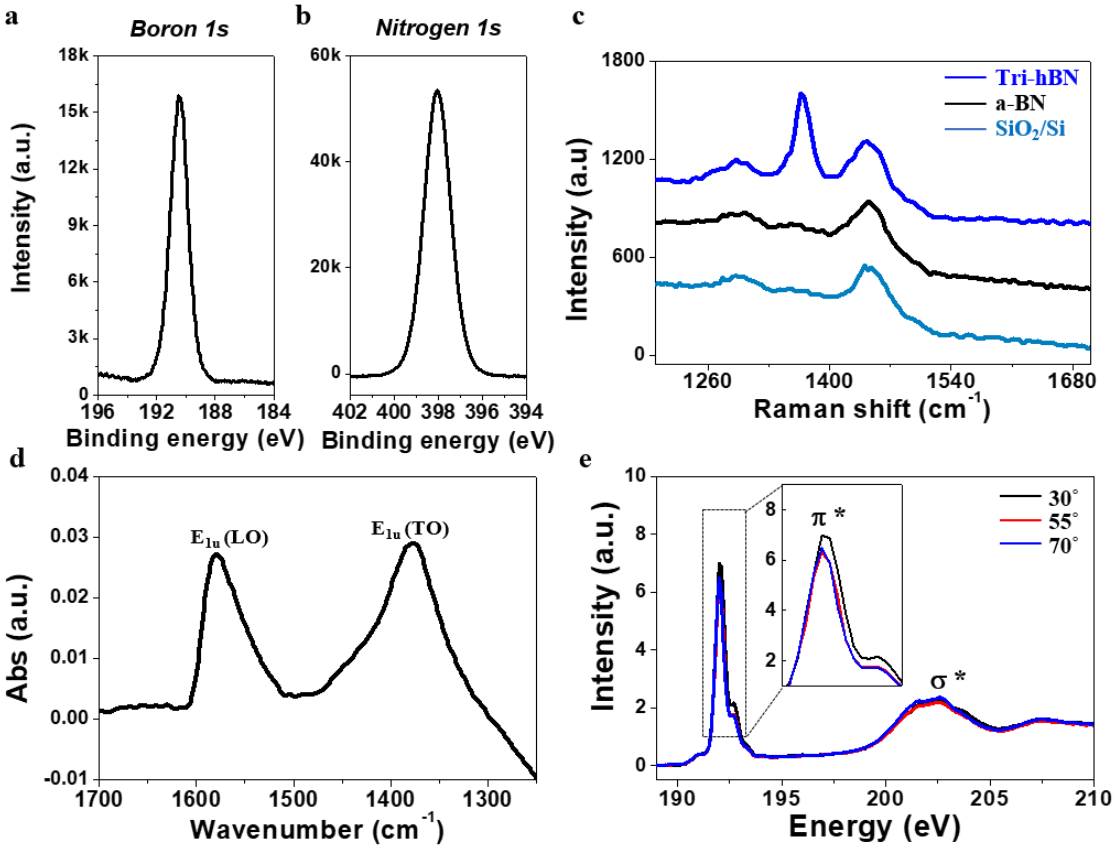

Fig. 2 | Chemical structure of a-BN. XPS profiles for (a) B 1s and (b) N 1s peaks; (c) Raman spectra of a-BN and epitaxially grown tri-layer h-BN (used as reference) on SiO_2/Si. The Raman spectrum of bare SiO_2/Si substrate is identical to that of a-BN – suggesting that no distinct crystalline h-BN modes are present in a-BN.; (d) FT–IR spectrum measured using s-polarised radiation at an incident angle of 60°; (e) PEY-NEXAFS spectra for the B K-edge of a-BN, measured at incident angles of 30°, 55°, and 70° - showing no dependence on orientation.

Raman spectra of a-BN and crystalline tri-layer hexagonal-BN (for comparison) reveal that the h-BN E_{2g} mode at 1373 cm^{-1} is absent in a-BN (Fig. 2c).[17,18] Fourier transform infrared spectroscopy (FTIR) spectrum in Fig. 2d shows that there is an absorption peak near 1370 cm^{-1} that is attributed to the transverse optical mode of BN in a-BN. Another IR mode located near 1570 cm^{-1} confirms the amorphous nature of sp^2-bonded BN[19]. We do not observe any N–H or B–H bonds with FTIR (Extended Data Fig. 5). Detailed chemical and density analysis were

conducted with Rutherford Backscattering Spectroscopy (RBS) and Elastic Recoil Detection Analysis (ERDA) – the results of which are shown in Extended Data Fig. 6.

Angle-dependent near-edge X-ray absorption fine structure (NEXAFS) measured in partial electron-yield (PEY) mode at Pohang Light Source-II 4D beam line was used to investigate the chemical and electronic structures of a-BN. In NEXAFS, X-ray absorption excites core electrons of B and N to unoccupied states— that is, 1s electrons are excited to empty π* and/or to σ* states. In the 1s → π* transition, the spatial orientation of π orbitals strongly impacts the transition probability. Thus, information pertaining to the relative orientation of orbitals in h-BN layers can be obtained by varying the incidence angle of X-rays.[20] NEXAFS spectra obtained for a-BN sample at incident angles of 30°, 55°, and 70° are shown in Figs. 2(e). The observed resonance at 192 eV corresponds to the 1s → π* transition in boron.[20] The resonance intensity of the 1s → π* transition in a-BN demonstrates negligible variation with X-ray incidence angle [Fig. 2(e)] – strongly indicating that BN planes are randomly oriented throughout the material. Similar conclusions can be drawn from NEXAFS spectra of N *K*-edge (Extended Data Fig. 7). Additionally, NEXAFS confirms that a-BN is completely sp^2-hybridised.[20,21] For completeness, we also deposited BN films at different ICP – CVD parameters such as power, temperature and pressure. We found that temperature was the most important parameter with ideal amorphous BN film deposition occurring at 400ºC at 30W plasma power. Above this temperature we obtained nanocrystalline BN (nc-BN) as shown in Extended Data Fig. 8

We now discuss the dielectric properties of a-BN. The dielectric constant is a physical measure of how easily electric dipoles can be induced in materials by application of an electrical field. The κ value of air or vacuum is 1, but electric polarizability in solid state matter

arises from dipolar, atomic and electronic components that are most relevant for high performance electronics. The contributions from these can be measured as a function of frequencies ranging from 10-kHz–30-MHz. The relative dielectric constants (κ) for a-BN and h-BN, for comparison, at different frequencies are shown in Fig. 3a. It can be seen that κ-values at 100 kHz are 3.28 and 1.78 for h-BN and a-BN, respectively. The values are average of measurements on > 50 devices. The distribution of measured values and the corresponding error bars at 100kHz are provided in Fig. 3b and Table I. Remarkably, at 1 MHz frequency, the observed κ–value for a-BN further reduces to 1.16, which is close to the value of air or vacuum. The low κ values of a-BN are attributed to nonpolar bonds between BN and also absence of order that prevents dipole alignment even at high-frequencies. The κ–values for a-BN compare extremely favourably to other reports in the literature, as shown in Extended Data Table 1. We have confirmed the electrical measurements of κ values with those obtained by measuring the refractive index of a-BN with spectroscopic ellipsometry and using the relationship: $n^2 = \kappa$.[22] The refractive indices of h-BN and a-BN at 633 nm wavelength were found to be 2.16 and 1.37, respectively, as indicated by the green stars in Fig. 3(b). Thus, κ-values for h-BN and a-BN from ellipsometry are 4.67 and 1.88, respectively – closely matching the values obtained with electrical measurements at 100kHz. Low-κ dielectric materials are sometimes made porous to exploit the low κ value of air but this decreases the density of the material, which in turn results in poor mechanical strength. It can be seen from Fig. 3c that a-BN possesses the lowest dielectric constant at the highest density in comparison with well-known low κ materials reported in the literature [Extended Data Table 1]. We have also measured the mechanical properties of a-BN films to confirm their strength. The results of nanoindentation measurements shown in Extended Data Fig. 9 indicates that the a-BN films possess hardness

and stiffness values that are equal to or greater than those of silicon (>11 GPa). The nanoscratch test results also shown in Extended Data Fig. 9 suggest that the films are very well adhered to the substrates.

The electrical breakdown strength of a-BN was extracted by measuring the current density with applied bias (Fig. 3d) on vertical sandwich type devices. The data in Fig. 3d reveal that there is a slight increase in current density due to Poole–Frenkel (P–F) tunnelling at low voltages and above 2.2 V, the leakage current sharply increases leading to electrical breakdown. As the thickness of a-BN is 3 nm, the breakdown field is extracted to be 7.3 MV-cm^{-1} – this is nearly twice that of h-BN (see Table I) and the highest reported for materials with dielectric constants of less than 2 as shown in Fig. 3e. The a-BN film also exhibits exceptionally low leakage current density of 6.27 μA/cm^2 at 0.3 V – thus, demonstrating its potential for 3 nm node devices. The key dielectric properties of a-BN and h-BN are summarised in Table 1.

Table 1. Electrical characteristics of a-BN and h-BN

	Electrical properties		Film properties	
	Dielectric constant @100 kHz / @1 MHz	Breakdown Field (MV-cm^{-1})	Reflective index (n) @ 633 nm	Density (g-cm^{-3})
h-BN	3.28 / 2.87	4.0	2.16	2.1
a-BN	1.78 / 1.16	7.3	1.37	2.1~2.3

A key step in back end of line (BEOL) CMOS fabrication of logic and memory devices is the deposition of a diffusion barrier between the low-κ dielectric material and the metal wire interconnects to prevent metal atom migration into the insulator. Ideally, this step can be eliminated if the low-κ dielectric material can also serve as the diffusion barrier. We have therefore tested the diffusion barrier properties of a-BN by depositing 80 nm of cobalt film on

a-BN and annealing the Co/a-BN/Si devices in vacuum for 1 h at 600 °C. This annealing condition is extremely harsh and under similar conditions severe diffusion of cobalt in Si occurs when industry standard TiN is used as the barrier layer (Extended Data Fig. 10). In contrast, no diffusion of Co or silicide formation was observed with a-BN in cross-sectional TEM results shown in Fig. 3f (additional data in the form of energy dispersive spectroscopy composition maps are shown in Extended Data Fig. 11) – suggesting that a-BN can serve as both the low-κ dielectric and the diffusion barrier. The comparison of breakdown bias in Co/a-BN/Si and Co/TiN/Si devices measured at various temperatures suggest that films are stable at high temperatures (Extended Data Fig. 12). Our results suggest that a-BN is an excellent low-κ material for high performance CMOS electronics.

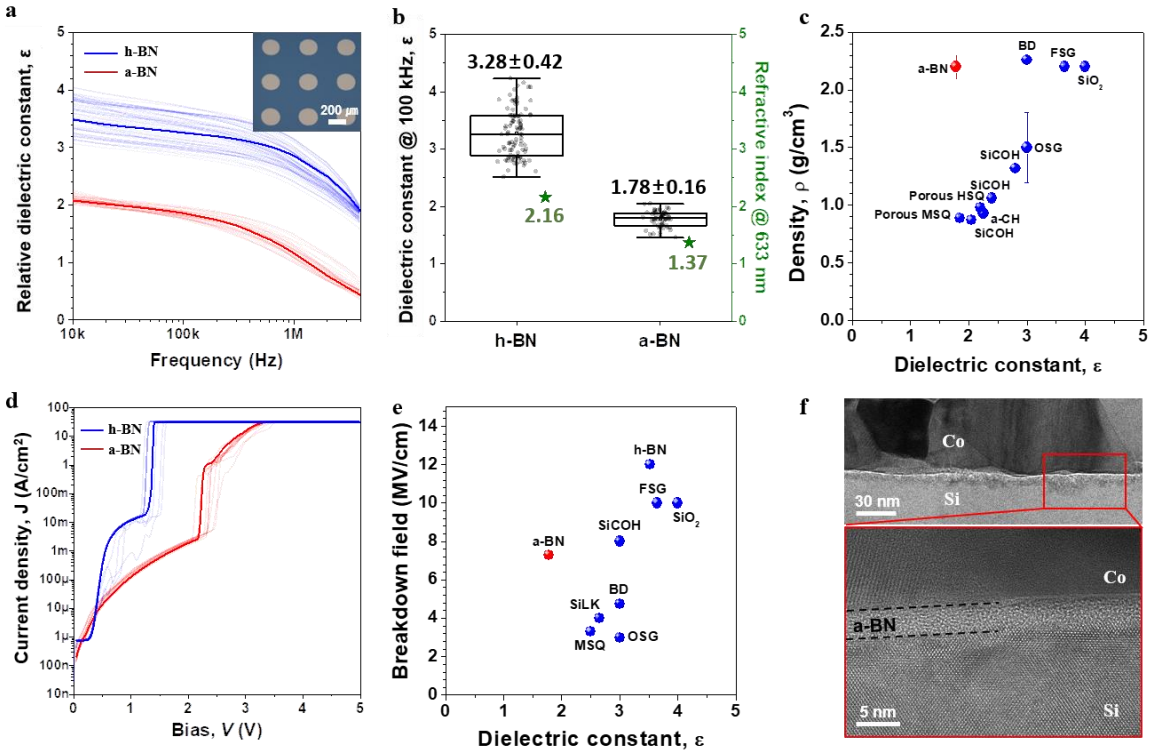

Fig. 3 | Dielectric properties of a-BN. (a) Dielectric constant determined using capacitance–frequency measurements on metal–insulator–metal (MIM) structures (thick blue and red lines denote averages; inset illustrates optical image of MIM structure); (b) Distribution of dielectric

constant values at 100 kHz and refractive indices (green stars) calculated via ellipsometry measurements; (c) Density versus dielectric constant of low-κ materials reported in literature (blue circles) with red circle denoting a-BN reported in this study; (d) Typical current–voltage (J−V) curves for h-BN (approximately 1.2 nm thick; blue curve) and a-BN (3 nm thick; red curve) films; (e) Breakdown field versus dielectric constant for low-κ materials reported in literature (blue circles) with red circle denoting a-BN; (f) Cross-sectional TEM images of a-BN after thermal-diffusion test performed for 1 h at 600 °C. The bottom image shows magnified view of red box marked in upper image.

References

1 Shamiryan, D., Abell, T., Iacopi, F. & Maex, K. Low-k dielectric materials. *Mater Today* **7**, 34-39, (2004).

2 Moore's deviation. *Nature Nanotechnology* **12**, 1105, (2017).

3 Akinwande, D. *et al.* Graphene and two-dimensional materials for silicon technology. *Nature* **573**, 507-518, (2019).

4 The International Roadmap for Devices and Systems: 2017, 4.5. Interconnect Technology Requirements. (2017).

5 King, S. W. Dielectric Barrier, Etch Stop, and Metal Capping Materials for State of the Art and beyond Metal Interconnects. *Ecs J Solid State Sc* **4**, N3029-N3047, (2015).

6 del Alamo, J. A. Nanometre-scale electronics with III–V compound semiconductors. *Nature* **479**, 317-323, (2011).

7 Venema, L. Silicon electronics and beyond. *Nature* **479**, 309-309, (2011).

8 Franklin, A. D. Nanomaterials in transistors: From high-performance to thin-film applications. *Science* **349**, aab2750, (2015).

9 Koenderink, A. F., Alù, A. & Polman, A. Nanophotonics: Shrinking light-based technology. *Science* **348**, 516-521, (2015).

10 Liu, C. *et al.* Small footprint transistor architecture for photoswitching logic and in situ memory. *Nature Nanotechnology* **14**, 662-667, (2019).

11 Xiang, D., Liu, T. & Chen, W. Fused computing and storage in a 2D transistor. *Nature Nanotechnology* **14**, 642-643, (2019).

12 Grill, A. PECVD low and ultralow dielectric constant materials: From invention and research to products. *Journal of Vacuum Science & Technology B* **34**, 020801, (2016).

13 More Moore Roadmap - The International Technology Roadmap for Semiconductors 2.0 White Paper: 2015, 7. Interconnect Scaling, 15-16 page., (2015).

14 Joo, W. J. *et al.* Realization of continuous Zachariasen carbon monolayer. *Sci Adv* **3**, e1601821, (2017).

15 Liu, J. *et al.* Plasma deposition of low dielectric constant (k=2.2~2.4) Boron Nitride on methylsilsesquioxane-based nanoporous films. *Journal of Applied Physics* **96**, 6679-6684, (2004).

16 Glavin, N. R. *et al.* Amorphous Boron Nitride: A Universal, Ultrathin Dielectric For 2D Nanoelectronics. *Adv Funct Mater* **26**, 2640-2647, (2016).

17 Kim, G. *et al.* Growth of high-crystalline, single-layer hexagonal boron nitride on recyclable platinum foil. *Nano Lett* **13**, 1834-1839, (2013).

18 Jang, A. R. *et al.* Wafer-Scale and Wrinkle-Free Epitaxial Growth of Single-Orientated Multilayer Hexagonal Boron Nitride on Sapphire. *Nano Lett* **16**, 3360-3366, (2016).

19 Plass, M. F., Fukarek, W., Mändl, S. & Möller, W. Phase identification of boron nitride thin

films by polarized infrared reflection spectroscopy. *Appl Phys Lett* **69**, 46-48, (1996).

20 Kim, D. Y. *et al.* Role of hydrogen carrier gas on the growth of few layer hexagonal boron nitrides by metal-organic chemical vapor deposition. *AIP Advances* **7**, 045116, (2017).

21 Jiménez, I. *et al.* Core-level photoabsorption study of defects and metastable bonding configurations in boron nitride. *Physical Review B* **55**, 12025-12037, (1997).

22 Dharma-wardana, M. W. C. Relation of the refractive index to the dielectric constant containing Doppler-like spatial dispersion. *Journal of Physics A: Mathematical and General* **9**, L93-L97, (1976).

23 Ling, X. & Zhang, J. Interference Phenomenon in Graphene-Enhanced Raman Scattering. *The Journal of Physical Chemistry C* **115**, 2835-2840, (2011).

24 Plimpton, S., Crozier, P. & Thompson, A. LAMMPS-large-scale atomic/molecular massively parallel simulator. *Sandia National Laboratories* **18**, 43, (2007).

25 Los, J. *et al.* Extended Tersoff potential for boron nitride: Energetics and elastic properties of pristine and defective h-BN. *Phys Rev B* **96**, 184108, (2017).

26 Tersoff, J. Empirical interatomic potential for silicon with improved elastic properties. *Phys Rev B* **38**, 9902, (1988).

27 Matsunaga, K. & Iwamoto, Y. Molecular dynamics study of atomic structure and diffusion behavior in amorphous silicon nitride containing boron. *J Am Ceram Soc* **84**, 2213-2219, (2001).

28 Al-Ghalith, J., Dasmahapatra, A., Kroll, P., Meletis, E. & Dumitrică, T. Compositional and Structural Atomistic Study of Amorphous Si–B–N Networks of Interest for High-Performance Coatings. *The Journal of Physical Chemistry C* **120**, 24346-24353, (2016).

29 Kimura, K., Joumori, S., Oota, Y., Nakajima, K. & Suzuki, M. High-resolution RBS: a powerful tool for atomic level characterization. *Nuclear Instruments and Methods in Physics Research Section B: Beam Interactions with Materials and Atoms* **219-220**, 351-357, (2004).

30 Kitahara, A., Yasuno, S. & Fujikawa, K. Study of thin-film thickness and density by high-resolution Rutherford backscattering spectrometry and X-ray reflectivity. *Transactions of the Materials Research Society of Japan* **34**, 613-615, (2009).

31 Hatton, B. D. *et al.* Materials chemistry for low-k materials. *Materials Today* **9**, 22-31, (2006).

32 Cheng, Y.-L. & Lee, C.-Y. in *Nanoporous Materials Porous Low-Dielectric-Constant Material for Semiconductor Microelectronics* (2018).

33 Zhao, L. *et al.* Role of copper in time dependent dielectric breakdown of porous organo-silicate glass low-k materials. *Appl Phys Lett* **99**, (2011).

34 Volinsky, A. A., Palacio, M. L. B., & Gerberich, W. W. in *Materials Research Society Symposium - Proceedings "Incompressible" pore effect on the mechanical behavior of low-K dielectric films.* 567-572.

35 Das, A. *et al.* Characterisation and integration feasibility of JSR's low-k dielectric LKD-5109.

Microelectron Eng **64**, 25-33, (2002).

36 Chang, S. Y. *et al.* Mechanical property analyses of porous low-dielectric-constant films for stability evaluation of multilevel-interconnect structures. *Thin Solid Films* **460**, 167-174, (2004).

37 Li, H. Y. *et al.* Process improvement of 0.13 mu m Cu/Low K (Black Diamond (TM)) dual damascene interconnection. *Microelectron Reliab* **45**, 1134-1143, (2005).

38 Pang. B., Y. W., Lee. P., Naik. M. in *Semiconductor Fabtech* 285-289 (London : ICG Publishing, 1994-, 1999).

39 Nagendra, V. in *Nanoindentation in Materials Science Mechanical Characterization of Black Diamond (Low-k) Structures for 3D Integrated Circuit and Packaging Applications* Ch. 10, (2012).

40 Tyberg, C. *et al.* in *Polymers for Microelectronics and Nanoelectronics* Vol. 874 *ACS Symposium Series* Ch. 12, 161-172 (American Chemical Society, 2004).

41 Im, J., Townsend, P. H., Curphy, J., Karas, C. & Shaffer, E. O. in *Metallization of Polymers 2* (ed Edward Sacher) 53-60 (Springer US, 2002).

42 Grill, A. Plasma enhanced chemical vapor deposited SiCOH dielectrics: from low-k to extreme low-k interconnect materials. *Journal of Applied Physics* **93**, 1785-1790, (2003).

43 Brandrup, J., Immergut, E. H. & Grulke, E. A. *Polymer handbook*. 4th edn, (Wiley-Interscience, 2004).

44 Lee, H. J. *et al.* Structural characterization of porous low-k thin films prepared by different techniques using x-ray porosimetry. *Journal of Applied Physics* **95**, 2355-2359, (2004).

45 Laturia, A., Van de Put, M. L. & Vandenberghe, W. G. Dielectric properties of hexagonal boron nitride and transition metal dichalcogenides: from monolayer to bulk. *npj 2D Materials and Applications* **2**, 6, (2018).

Acknowledgements We thank Y. K. Kim from UNIST Central Research Facilities (UCRF) for cross sectional HR-TEM images. This work was supported by Samsung Electronics (Samsung-SKKU Graphene/2D Center), the research fund (NRF-2017R1E1A1A01074493 and NRF-2019R1A4A1027934) and the grant (CASE-2013M3A6A5073173) from the centre for Advanced Soft Electronics under the Global Frontier Research Program through the National Research Foundation by the Ministry of Science and ICT, Korea. The NEXAFS experiments were performed at 4D, 6D and 10A2 beamline of the Pohang Accelerator Laboratory (PAL) were supported in part by the Ministry of Science and ICT, POSTECH, and UNIST.

Author contributions H.S.S. and H.J.S. planned and supervised this project; S.H., K.Y.M., G.K, S.I.Y and H.S.S. performed experiments for growth and characterization.; C.-S.L., M.-H.L. and H.-J.S. fabricated electrical devices; S.W.K measured ellipsometry and analyzed; H.L. measured RBS and analyzed; Y.L. and Z.L. measured TEM data. K.I, K.K. and T.J.S. measured NEXAFS data; E.-C.J, H, H.J., and J.-Y.K measured mechanical property and adhesion; A.A. and S.R. performed MD simulations; MC advised on the project, wrote and edited the manuscript with H.S.S. All authors contributed to writing the manuscript and agreed on the content of the paper.

Competing interests The authors declare no competing interests.

Additional information

Supplementary information is available for this paper at www.nature.com/nature.

Correspondence and requests for materials should be addressed to H.S.S. or H.J.S.

Reprints and permissions information is available at www.nature.com/reprints.

Methods

Si-substrate cleaning:

Si substrates were ultrasonicated in acetone for 10 min and subsequently cleaned using iso-propenyl alcohol (IPA) and N_2 gas. Upon completion of the organic-solvent cleaning process that lasted 5 min, the Si substrates were subjected to O_2 plasma treatment to not only remove any carbon impurities remaining on the surface but also to make the surface hydrophilic and

enhance its wettability. Subsequently, the substrates were immersed in 10% dilute HF solution for 10 min to remove native oxide. Finally, anhydrous ethanol and N_2 gas were used to remove residual HF solution from the surface.

Growth of a-BN:

The clean Si substrates were placed inside the inductively coupled plasma chemical vapour deposition (ICP-CVD, Extended Data Fig. 1) system at centre of the furnace. Borazine (purchased from Gelest) precursor flask was placed in a water bath at -15 °C. The temperature during use was ramped up to 25 °C. For uniform growth, the substrate was tilted by ~ 30° using a Cu support. Prior to ramping up the furnace temperature, pressure inside the CVD system was reduced to its base value of 1×10^{-4} torr and 20 sccm of H_2 gas was introduced. Subsequently, the furnace temperature was increased at the rate of 10 °C/min to a set target value (400 °C for a-BN), which was maintained for 20 min before starting the deposition. During the growth period, plasma generation was performed at 30-W power by activating the ICP (inductively coupled plasma) unit under a flow of borazine gas at 0.05 standard cubic centimetre per minute (sccm, controlled by mass flow controller). Growth was conducted for 90 min. At the end of the deposition, the borazine flow and plasma generation were terminated, and the furnace was cooled to room temperature using 20 sccm of H_2 gas.

Transfer technics of samples:

To transfer a-BN films, hydrofluoric acid transfer technique described in Ref 18 employed here.

Characterisation:

Scanning electron microscopy (SEM; Verios 460; FEI) and atomic force microscopy (AFM; Dimension Icon; Bruker) were used to determine sample surface morphologies. XPS (K-Alpha; Thermo Fisher) observations were performed to determine chemical composition. Raman spectra were measured using a micro Raman spectrometer (alpha 300; WITec GmBH) equipped with a 532 nm laser. To obtain accurate Raman spectra, samples were transferred on SiO_2 (300 nm)/Si substrates to amplify the Raman signal by multiple reflections.[23] FT–IR spectra were acquired using a Varian FT-IR 670 spectrometer equipped with a Seagull variable angle reflection accessory. Incident light was polarised using a wire-grid polariser. NEXAFS analysis was performed using the 4D PES beamline at the Pohang accelerator laboratory in

Korea. During NEXAFS analysis, samples were attached to a molybdenum holder and loaded into a vacuum chamber. The analysis chamber, maintained at a base pressure of 5×10^{-10} Torr, was equipped with an electron analyser (R3000; Scienta) and X-ray absorption spectroscopy detector having a retarding filter for facilitating operation in the partial electron-yield mode. For high-resolution imaging and selected area electron diffraction (SAED), low-voltage Cs aberration-corrected transmission electron microscope (Titan Cube G2 60-300; FEI) was performed at 80 kV using a monochromatic electron beam. To facilitate sample observation using TEM, a-BN was transferred on to SiN TEM grids (hole diameter: 1 μm). High-resolution cross-sectional transmission electron microscopy (JEM-2100F; JEOL) was performed to confirm the barrier performance.

Molecular dynamic simulations and computations:

We modelled the Si substrate using a 6-layer diamond cubic rectangular slab whose free surface is perpendicular to the *z*-axis for BN nucleation and growth. The slab was periodic in the xy-plane with 18x18 repetition of the unit cell, with a total of 15552 Si atoms. The top five layers were completely unrestrained during the simulations, while the bottom layer was kept fixed. The system contains 8211 atoms of Boron and Nitrogen in a 1:1 ratio with an additional amount of 400 H atoms (~5%) to be consistent with the experimental observations. All the simulations were performed using LAMMPS.[24] Throughout the simulation the temperature of the substrate is held constant using a Nosé-Hoover thermostat in an NVT ensemble at T=673 K. A wall with a harmonic repulsive potential is placed 25 Å above the substrate. The film is grown using the following method: all the atoms (Boron, Nitrogen and Hydrogen) are initialized with random velocities in a region of 20 Å above the substrate. They are constantly thermalized at the growth temperature and allowed to settle and cool on the Si substrate. To prevent premature B-N bond formation, the minimal distance between the initial B and N sources was set to be 1.90 Å, larger than the B-N bond length of 1.44 Å in the h-BN lattice. The equation of motion was numerically solved using the velocity-Verlet integration scheme. Each simulation was run for more than 15 ns at a time step of 0.25 fs. After the growth process, the systems were further relaxed in a NPT ensemble at T= 300 K. The extended Tersoff potential for BN was employed to describe the chemical processes (e.g. bond formation and dissociation) among the atomic species involved.[25] This model potential has been specifically designed to correctly describe the dependence on coordination and chemical environment of the bonding occurring in B, N and

B-N systems. Thanks to its versatility, it allows to describe large scale atomistic simulations whose number of atoms exceeds a few thousands. To describe the interaction within the Silicon substrate we used the Tersoff model potential which has been proved to faithfully reproduce both mechanical and morphological properties of silicon-based systems.[26] We treated the Si-N and Si-B interactions via the Tersoff potential parameterized,[27] which has been already employed to study the compositional and structural features of Si-B-N networks.[28] Finally, we modelled all the interactions involving Hydrogen through a Lennard-Jones potential.

Ellipsometry:

An automated angle M-2000F rotating compensator ellipsometer equipped with an X–Y mapping stage, focusing probes, and accompanying software—Complete-EASE 6.39 from J.A. Woollam Co., Inc. was used in this study. Ellipsometric data were acquired in the wavelength range 250–1000 nm wavelength range with a 1.6 nm resolution at incidence angles of 65°, 70°, and 75°. Optical properties of both films were determined using the Kramers–Kronig consistent dispersion model involving use of 3 Lorentz oscillators.

High-resolution Rutherford backscattering and high-resolution elastic recoil detection analysis:

To investigate element compositions of the two ultra-thin films considered in this study, high-resolution Rutherford backscattering spectrometry (HR-RBS) was employed.[29] The said HR-RBS analysis was performed by irradiating samples using a 450-keV He^+ beam generated by HRBS-V5000 (KOVELCO). Employing the same system, high-resolution elastic recoil detection analysis (HR-ERDA) was simultaneously performed for hydrogen using 500-keV N^+ ions. Typical beam-current values during HR-RBS and HR-ERDA analyses equalled 40 nA and 6 nA, respectively.

Density measurement:

Peaks corresponding to elements—B, N, O and Si—were observed individually in the HR-RBS spectra. Areas covered by the peaks reflect both the thickness and density simultaneously. The areal density (atoms/cm^2) was measured,[30] which in turn, facilitated calculation of the a-BN film density by considering their thicknesses. Note that the presence of oxygen was observed owing to surface contamination.

Breakdown-voltage and dielectric-constant measurement:

J–V and C–f (capacitance–frequency) characteristics of the films with metal/a-BN/n-Si stacks were measured using a Tektronics K4200A-SCS parameter analyser system and Karl Suss PA-200DS semi-auto probe station. a-BN-based capacitors were fabricated on directly-deposited or transferred BN films on n-Si substrates. To prevent polymer contamination, a shadow mask with 200-μm diameter pattern was used, and a 100 nm Cu electrode was deposited over the a-BN–Si stack. Post device fabrication, capacitance–voltage units (CVU) within K4200A-SCS were first employed to facilitate C–f measurement. We carried out capacitance-frequency measurements in a frequency range of 1 kHz to 10 MHz with a 0.5 V hold bias and ± 30 mV AC drive. Measured capacitance values do not demonstrate a significant change as a function of the applied voltage of 0.5 V. Therefore, the relative dielectric constant was evaluated using the relation $\kappa = Ct/A\varepsilon_0$, where C denotes capacitance, t denotes a-BN-film thickness, A denotes area, and ε_0 denotes the dielectric constant. At high frequencies exceeding 5 MHz, significant noise levels were observed in the capacitance owing probably to low impedance of the a-BN capacitor. Subsequently, J–V characteristics of both film samples were determined using source-measurement units (SMUs) within K4200A-SCS. The applied-voltage value was swept from 0 to 10 with 1 pA resolution and 10-mA compliance current. Additionally, measurements were in 50 mV current steps and 10 NPLC (number of power line cycles) to prevent degradation due to bias stresses.

Diffusion-barrier performance estimation:

To evaluate the diffusion-barrier performance of films considered in this study, approximately 3 nm thick samples of a-BN and TiN (RF sputtering) were deposited on a Si substrate. Subsequently, the samples were coated with an 80 nm Co layer using DC sputtering. Post deposition, samples were placed inside a furnace for annealing. The furnace temperature was ramped up at a high rate of 40 °C/min. During annealing, thermally activated diffusion was observed to occur at the interface between Co and dielectric barrier materials.

Data availability

The datasets generated and/or analysed during the current study are available from the corresponding author on reasonable request.

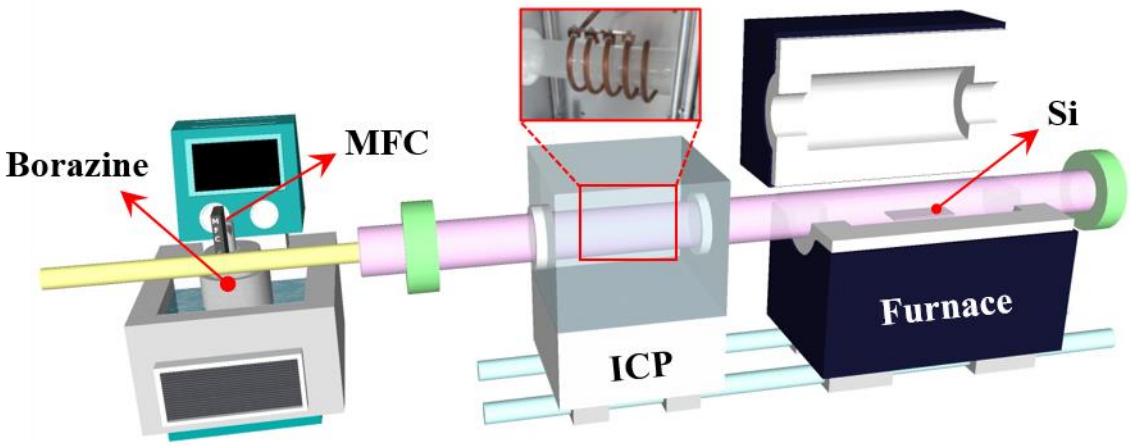

Extended Data Fig. 1 | (a) ICP-CVD system with borazine mass flow controller (MFC) for precise control of borazine flow. The a-BN films were grown on Si substrates at 400 °C.

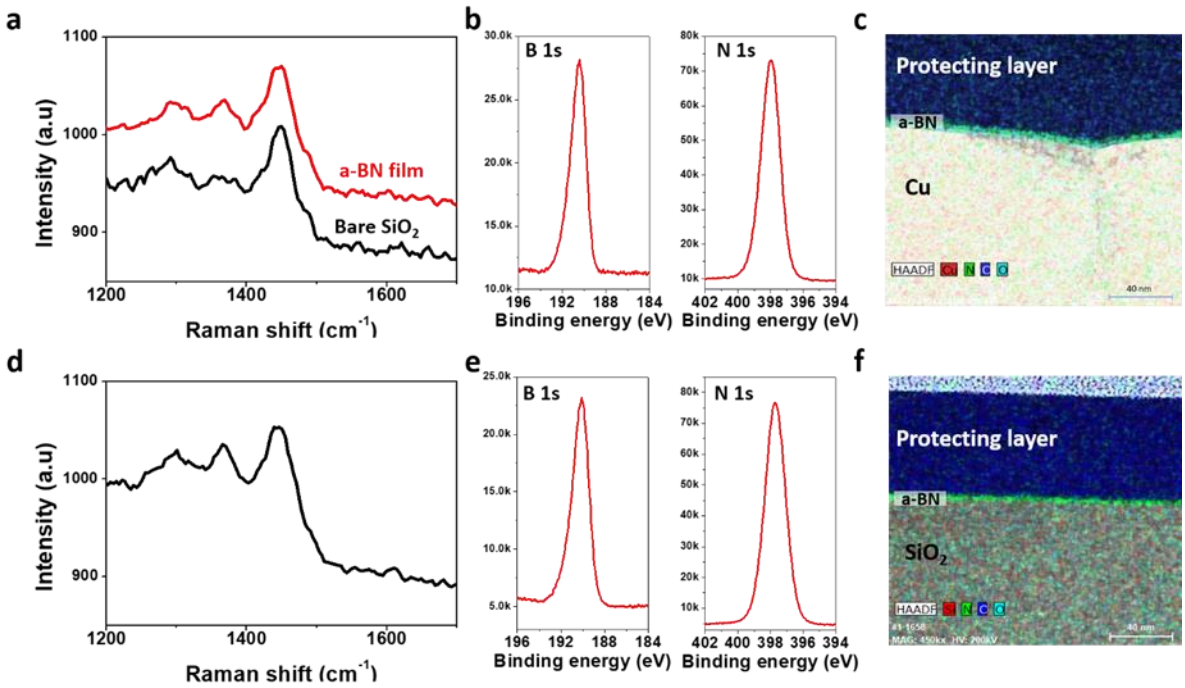

Extended Data Fig. 2 | (a-c) Raman, XPS, and EDS mapping image of a film grown on copper foil (30W plasma power, Growth Temp = 300 ºC) and transferred onto SiO_2 substrates so that Raman could be measured. The Raman spectrum on the aBN film is similar to those of bare amorphous SiO_2 – similar to spectra on Si reported in our original paper. (d-f) Raman, XPS, and EDS image of a film grown directly on SiO_2 (10W plasma power, Growth Temp = 200 ºC). The spectra are largely the same for all substrates. The dielectric properties obtained from spectroscopic ellipsometry reveal no influence of substrate since the structure and composition of the films is similar in all cases. Scale bar is 40 nm.

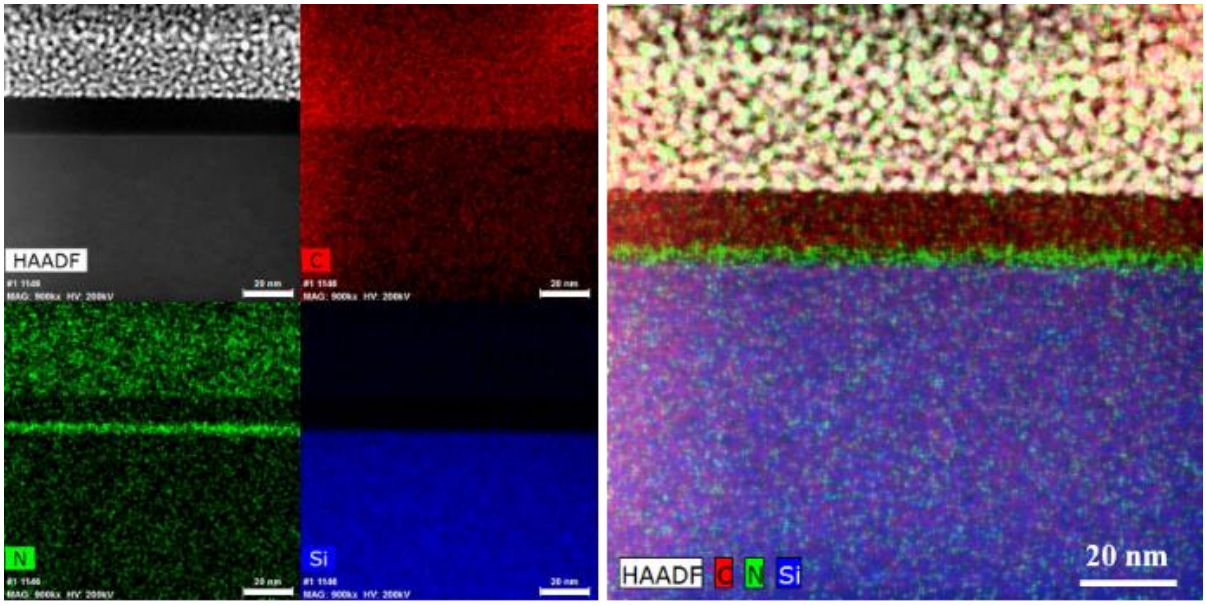

Extended Data Fig. 3 | High angle annular dark field (HAADF)-STEM (left) image overlaid with energy dispersive spectroscopy (EDS) mapping of carbon (red), nitrogen (green), and silicon (blue). EDS overlapped image (right) for all elements is shown on the right. Scale bars = 20 nm.

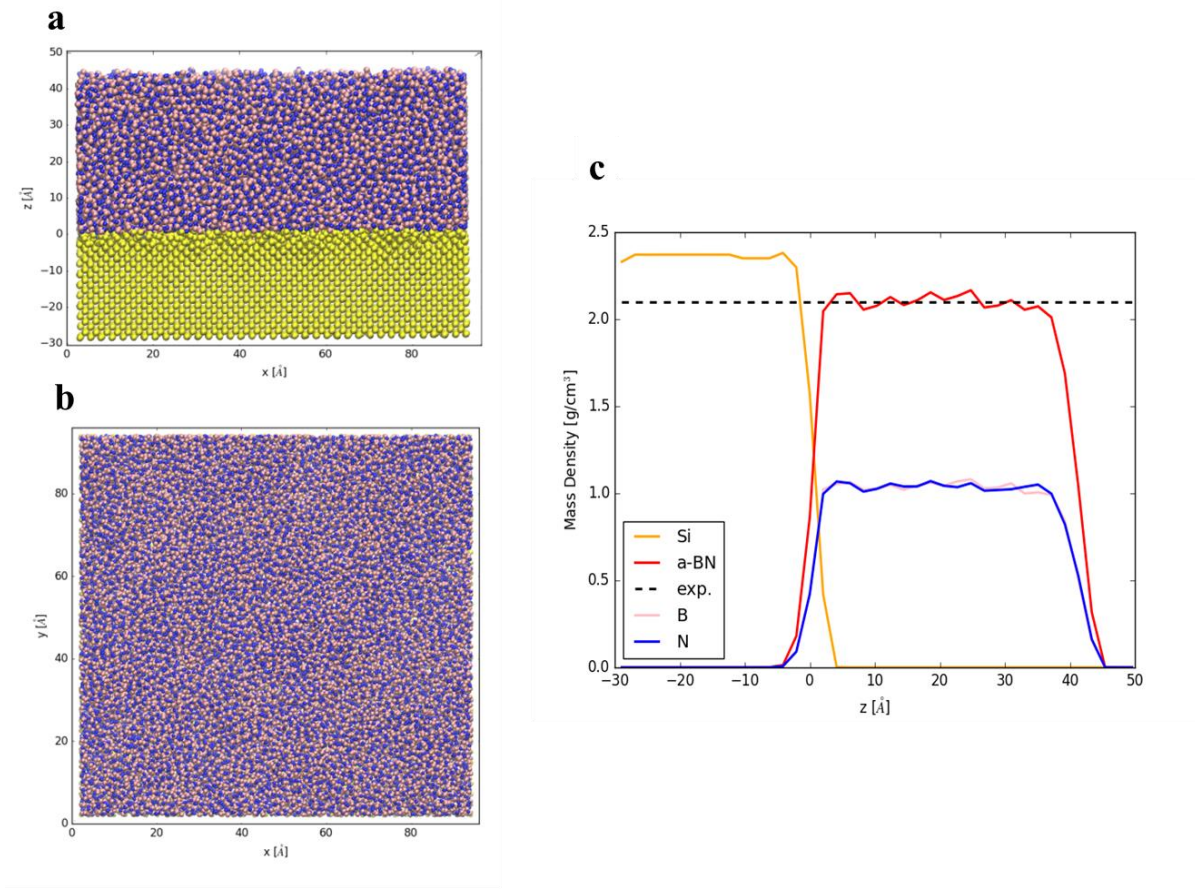

Extended Data Fig. 4 | Image of a -BN sample grown on a Si substrate at T= 673K: a) side view, b) top view. Atomic species are shown in different colours: Si (yellow), Blue (N), Pink (B). (c) Mass density profile along the transverse direction (z-direction) in the system of (a) and (b). Different colours denote densities of different chemical species. The simulated density of a-BN is consistent with the experimental result obtained in this study. The black dashed line corresponds to the BN mass density from experimental measurements.

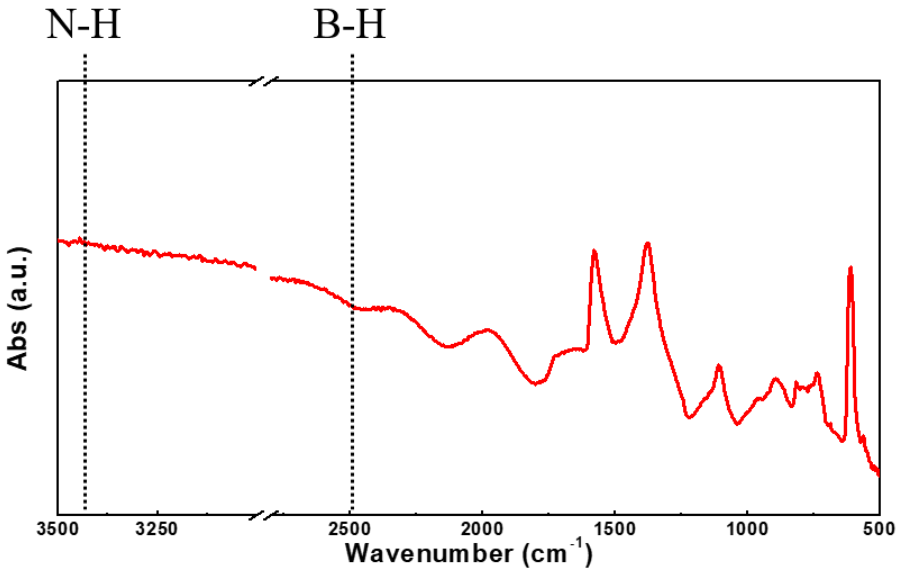

Extended Data Fig. 5 | FTIR spectra for a-BN showing the absence of B-H and N-H.

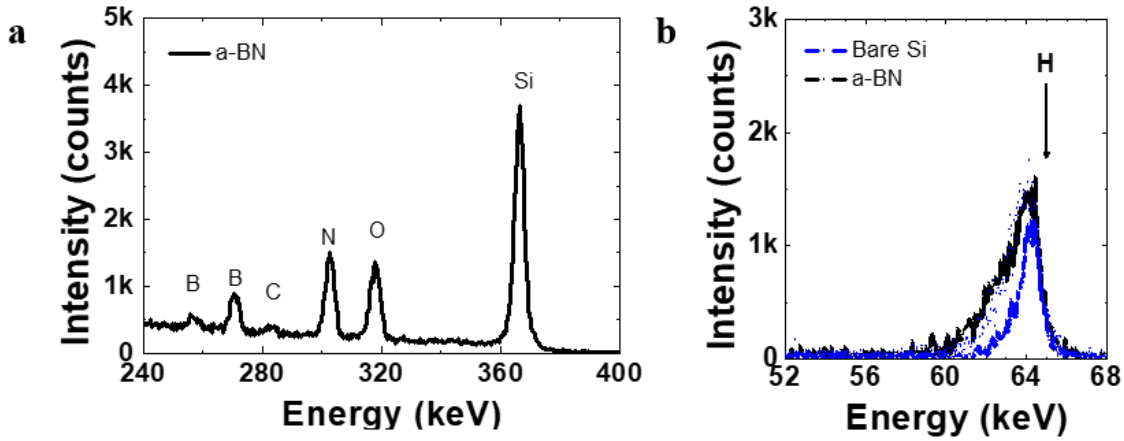

c

Samples	B (at%)	N (at%)	H (at%)
a-BN	47.6	46.9	5.5

Extended Data Fig. 6 | (a) HR-RBS and (b) HR-ERDA spectra for a-BN film within energy ranges of 240–400 keV and 52–68 keV, respectively; (c) Element composition calculated using HR-RBS and HR-ERDA spectra.

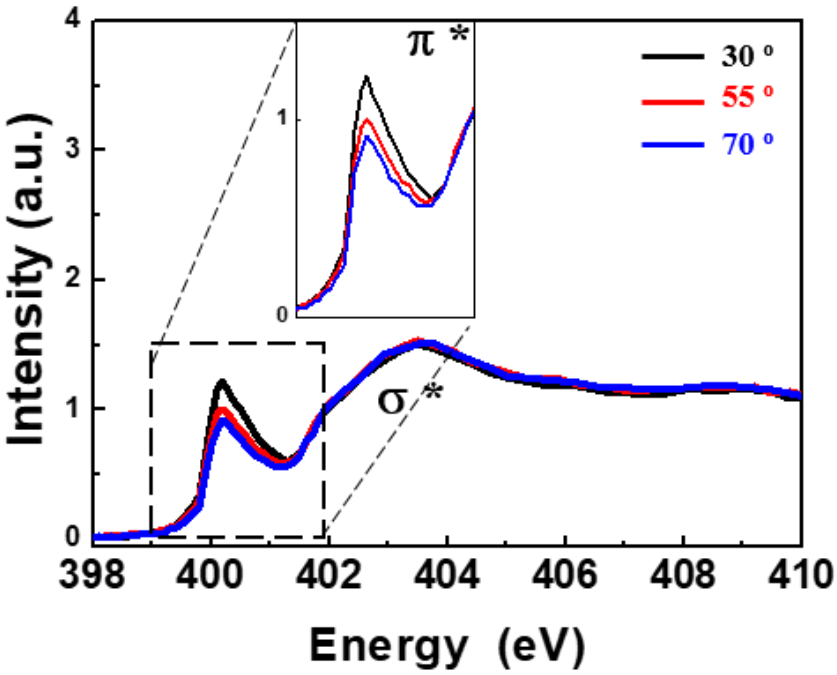

Extended Data Fig. 7 | Partial electron yield near-edge X-ray absorption fine structure (PEY-NEXAFS) spectra for N K-edge of a-BN, demonstrating trivial angle dependency of N K-edge.

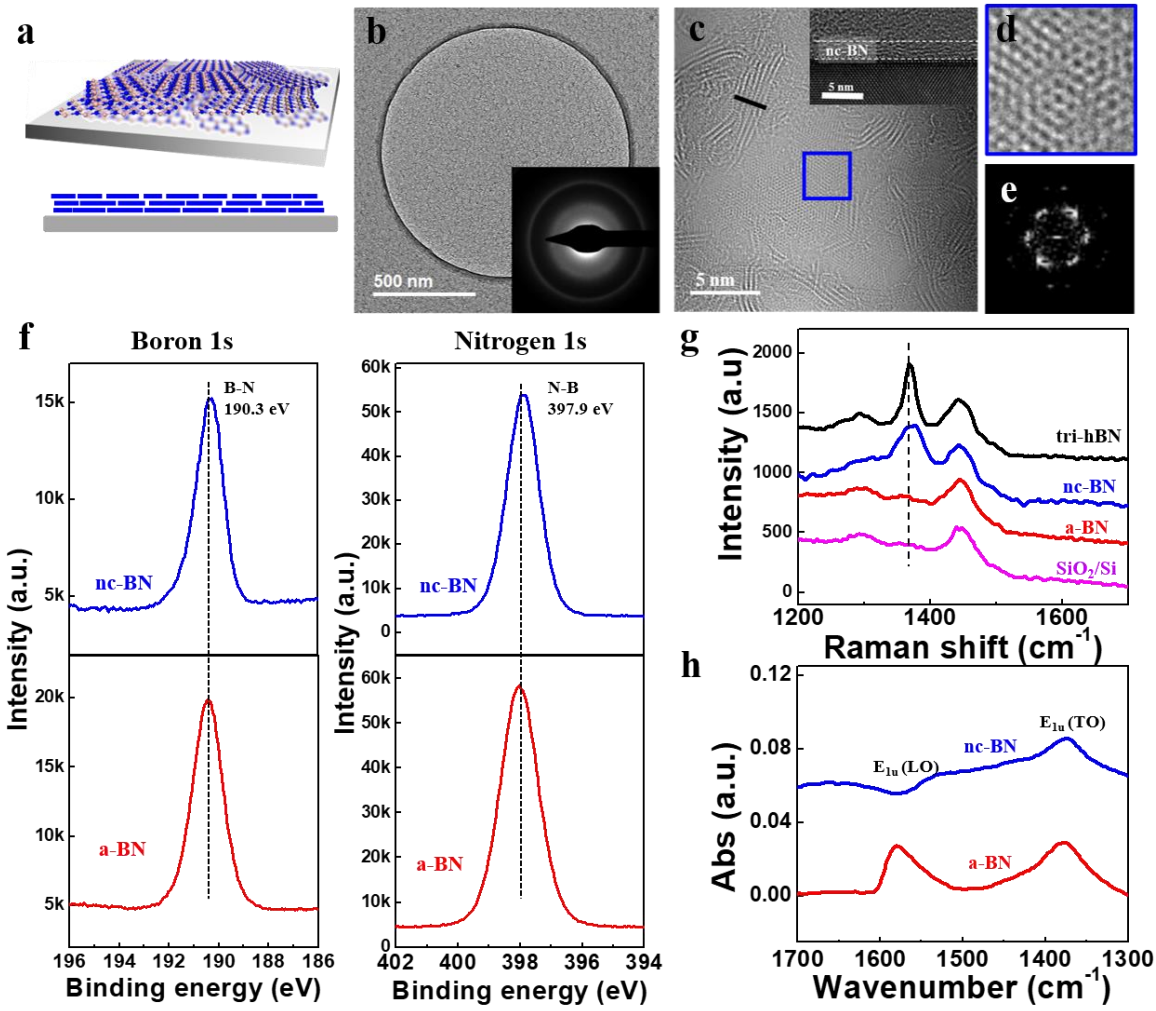

Extended Data Fig. 8 | Comparison of a-BN and nanocrystalline BN (nc-BN) films. (a) Schematic of the nc-BN film structure deposited at 700 ºC. (b) Low magnification TEM images of nc-BN. (Selected area electron diffraction pattern in the inset shows a typical polycrystalline ring pattern) (c) High resolution TEM images of nc-BN clearly shows small crystallites of h-BN. (Cross sectional TEM image in the inset indicates a layered structure) (d) Magnified image of (c) blue box area and (e) FFT image show hexagonal superstructure of multilayer h-BN. (f) XPS profiles for B 1s and N 1s peaks observed in 3-nm-thick a-BN and nc-BN samples. (g) Raman spectra for a-BN, nc-BN, and epitaxially grown tri-layer h-BN (used as reference and measuring 1.2-nm thick) samples transferred onto SiO_2/Si substrates. (h) FT–IR spectra for a-BN (red line) and nc-BN (blue line) measured using s-polarised radiation at an incident angle of 60°. (E_{1u} LO mode related with amorphous of BN, see ref. 19)

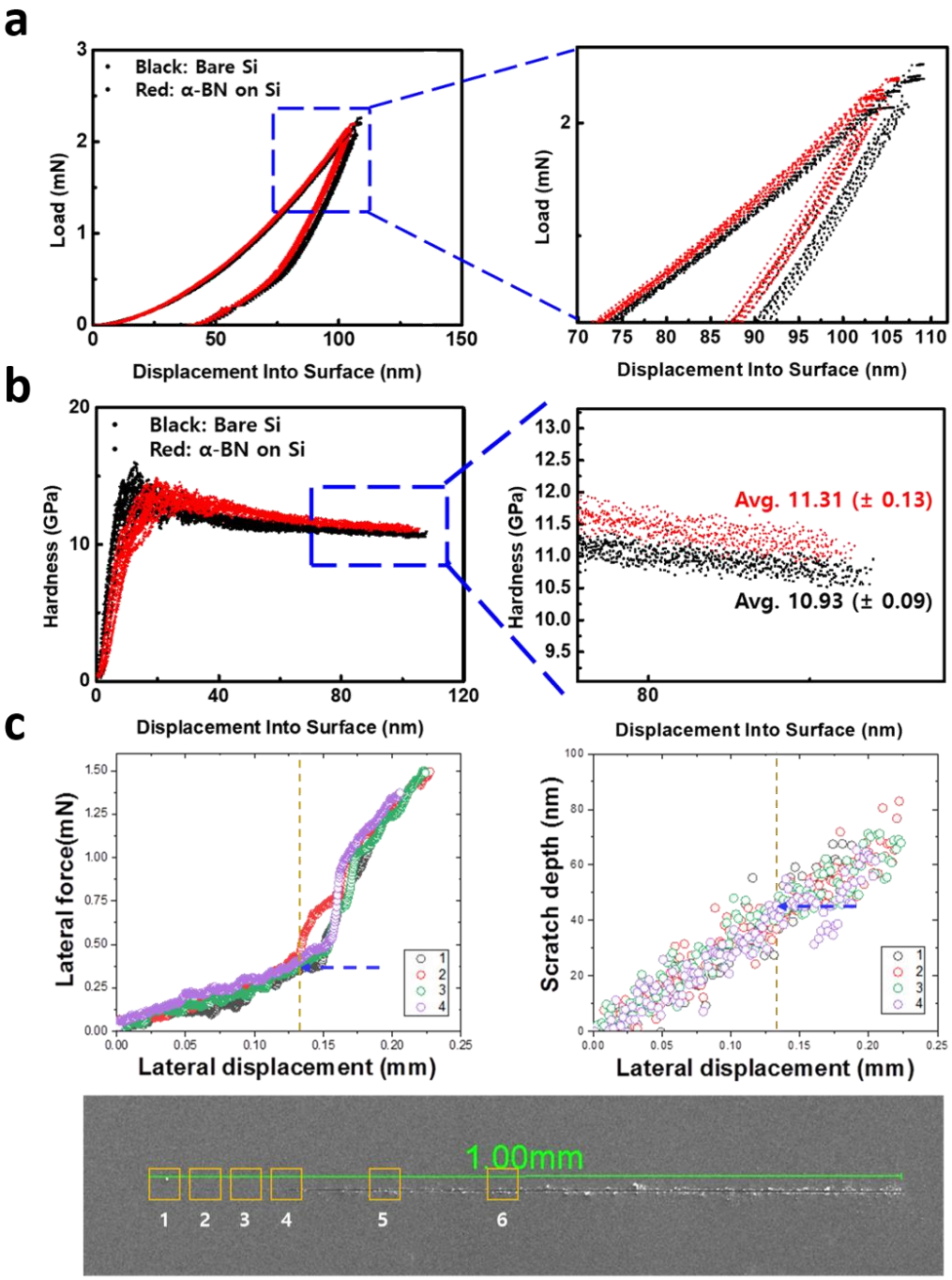

Extended Data Fig. 9 | (a-b) Nanoindentation results show that deposition aBN on Si substrates leads to enhancement in surface hardness and stiffness. (c) Nanoscratch test results reveal that scratch depth of 40 nm (>10 times the film thickness) is required to delaminate the film – suggesting excellent adhesion with Si substrate. SEM observations show that the scratch regions are clean and no evidence for delamination of aBN can be found for scratch depth shallower than 40 nm.

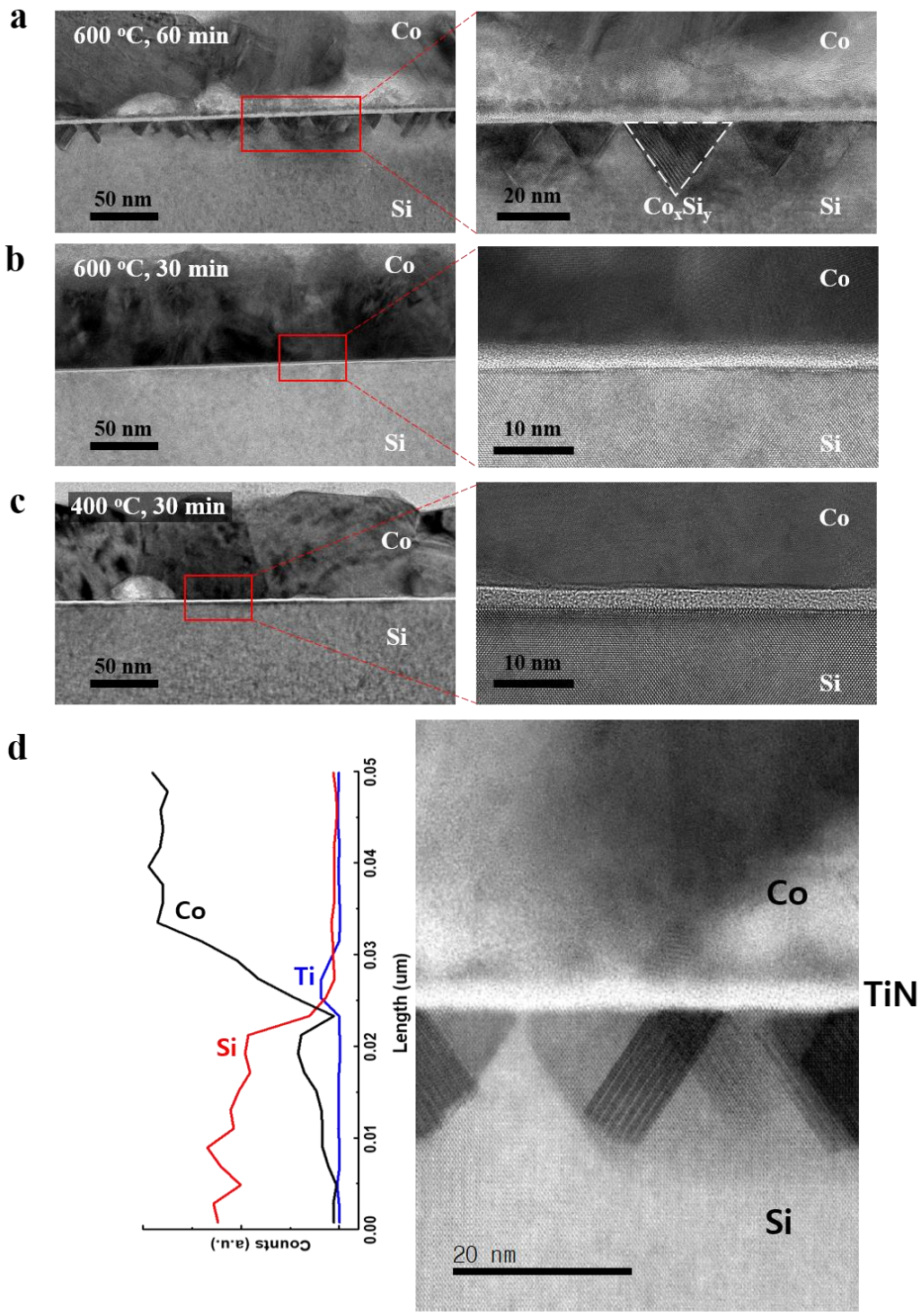

Extended Data Fig. 10 | Cross-sectional TEM images of Co (80 nm)/TiN (3 nm)/Si films after thermal diffusion tests at different temperatures: (a) 600 °C for 60 min, (b) 600 °C for 30 min, (c) 400 °C for 30 min, and (d) enlarged cross-sectional TEM image and EDS line profile in (a).

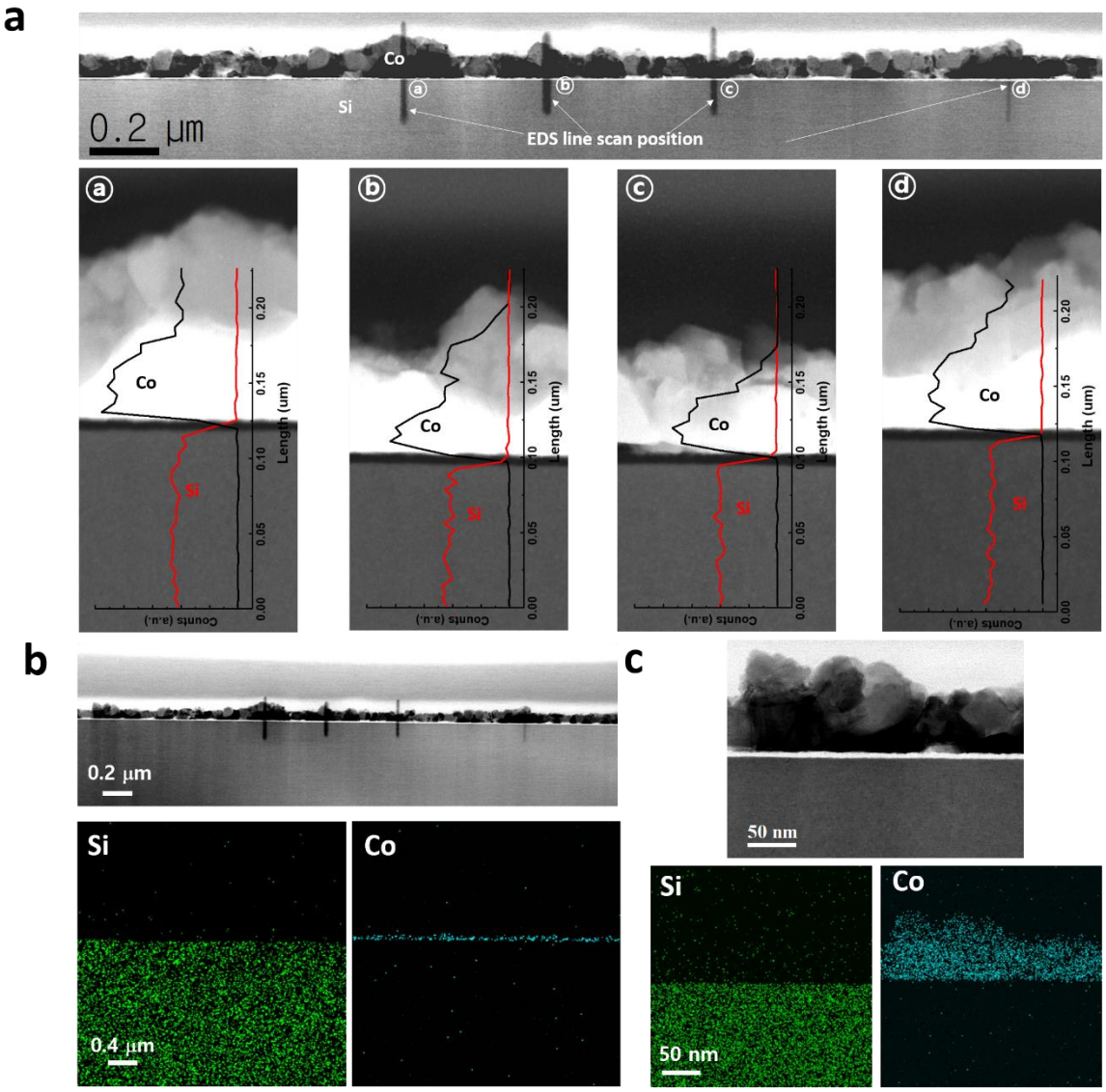

Extended Data Fig. 11 | (a) Large-area cross-sectional TEM image and EDS line profiles of Co/a-BN(3 nm)/Si sample after annealing at 600 ºC for 60 min. (b) EDS maps of Co and Si showing that Co is isolated above the aBN film and does not diffuse into the Si. (c) EDS maps of a magnified area in (b).

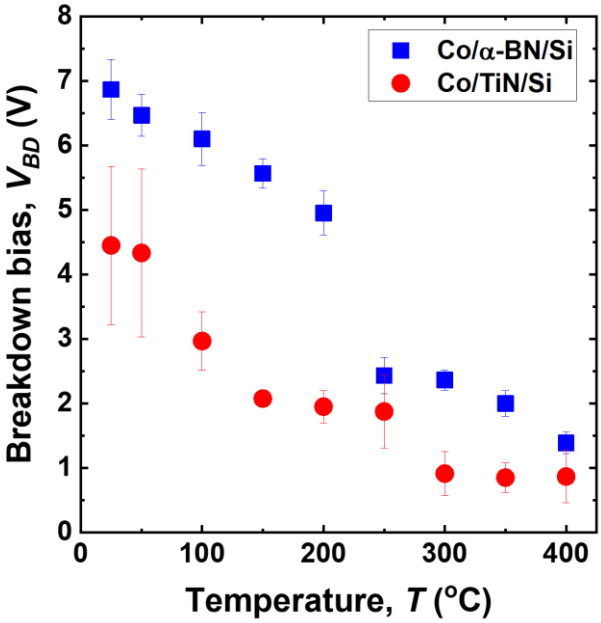

Extended Data Fig. 12 | Comparison of breakdown bias at different temperatures for a-BN and TiN barriers.

Extended Data Table 1 | Comparison of dielectric constants of various dielectric materials

	Dielectric constant	Density (g/cm^3)	Modulus (GPa)	Hardness (GPa)	Breakdown field (MV/cm)	
SiO_2	4	2.2	55~70	3.5	>10	Ref. [31,32]
FSG (Fluorinated silicon glass)	3.5~3.8	2.2	~50	3.36	>10	Ref. [31,32]
OSG (organosilicate glass or carbon-doped silicon glass)	2.8~3.2	1.8~1.2	6.6~8.4	1.2~1.7	3.0 Ref. [33]	Ref. [31,32,34]
HSQ	~3.0					
MSQ	~2.5		2.7~12.5	0.19~0.936	3.3 Ref. [35]	Ref. [36]
Black Diamond (SiCOH)	2.7~3.3	<2.26	10~20	1.5~3.0	4.75 Ref. [37]	Ref.[38,39]
$Si_wC_xO_yH_z$	2.7~3.0		9~15	1.3~2.4	6~10	Ref. [40]
SiLK	2.65		2.7	0.38	4	Ref.[40,41]
SiCOH	2.8	1.32	16.2	1.69		Ref. [42]
pSiCOH (pore <1.5 nm)	2.4	1.06	4.2	0.28		Ref. [42]
pSiCOH (pore <2.5 nm)	2.05	0.87	3.3	0.28		Ref. [42]
$a\text{-}CH_{polymeric}$	2.2~2.3	0.92~0.94				Ref.[34,43]
Porous HSQ (hydrogen silsesquioxane) (porosity 46%)	2.2	0.98				Ref. [44]
Porous MSQ (methylsilsesquioxane) (porosity 34%)	1.85	0.89				Ref. [44]
BCN (boron carbon nitride)	3.7~4.6					Ref. [5]
h-BN	3.29~3.76	2.1	19.5~100	0.6~3		Ref. [45]
a-BN or amorphous h-BN	2.2~2.4 5.9					Ref.[15] Ref.[16]
a-BN	1.16~1.78	2.1~2.3			7.3	This work